Ocean Modelling 92 (2015) 69–84

Contents lists available at ScienceDirect

Ocean Modelling

journal homepage: www.elsevier.com/locate/ocemod

The seasonal cycle of submesoscale flows

Liam Brannigan[a,*], David P. Marshall[a], Alberto Naveira-Garabato[b], A.J. George Nurser[c]

[a] *Atmospheric, Oceanic & Planetary Physics, Clarendon Lab, University of Oxford, Oxford, England*
[b] *University of Southampton, National Oceanography Center, Southampton, England*
[c] *National Oceanography Center, Southampton, England*

ARTICLE INFO

Article history:
Received 9 December 2014
Revised 21 April 2015
Accepted 4 May 2015
Available online 22 May 2015

Keywords:
Submesoscale
Mixed layer fronts
Frontogenesis
Symmetric instability
Baroclinic instability
Seasonal cycle

ABSTRACT

The seasonal cycle of submesoscale flows in the upper ocean is investigated in an idealised model domain analogous to mid-latitude open ocean regions. Submesoscale processes become much stronger as the resolution is increased, though with limited evidence for convergence of the solutions. Frontogenetical processes increase horizontal buoyancy gradients when the mixed layer is shallow in summer, while overturning instabilities weaken the horizontal buoyancy gradients as the mixed layer deepens in winter. The horizontal wavenumber spectral slopes of surface temperature and velocity are steep in summer and then shallow in winter. This is consistent with stronger mixed layer instabilities developing as the mixed layer deepens and energising the submesoscale. The degree of geostrophic balance falls as the resolution is made finer, with evidence for stronger non-linear and high-frequency processes becoming more important as the mixed layer deepens. Ekman buoyancy fluxes can be much stronger than surface cooling and are locally dominant in setting the stratification and the potential vorticity at fronts, particularly in the early winter. Up to 30% of the mixed layer volume in winter has negative potential vorticity and symmetric instability is predicted inside mesoscale eddies as well as in the frontal regions outside of the vortices.

1. Introduction

The upper ocean stratification is an important control on the transfer of momentum and tracers between the atmosphere and ocean interior. The development of upper ocean stratification has historically been viewed as a one-dimensional process driven by surface buoyancy and frictional fluxes, with allowance for shear-driven mixing at the base of the mixed layer. These ideas are encapsulated in a number of one-dimensional parameterisation schemes for the surface boundary layer (e.g. Price et al., 1986; Large et al., 1994). Attention has since focused on the role a number of other processes play in setting upper ocean stratification such as geostrophic adjustment (Dale et al., 2008; Tandon and Garrett, 1994), frontogenesis (Gula et al., 2014; Hoskins and Bretherton, 1972; Lapeyre et al., 2006; Shakespeare and Taylor, 2013), surface waves and Langmuir turbulence (Belcher et al., 2012; Grant and Belcher, 2009; Hamlington et al., 2014; Haney et al., Subm. to JPO; McWilliams and Fox-Kemper, 2013; Sutherland et al., 2014), Ekman buoyancy fluxes (hereafter EBF, Thomas, 2005; Mahadevan, 2006; Thomas and Ferrari, 2008; Thomas et al., 2013), symmetric and inertial instabilities (Bachman and Taylor, 2014; D'Asaro et al., 2011; Haine and Marshall, 1998; Thomas and Taylor, 2010; Thomas et al., 2013; Thomsen et al., 2013), and mixed layer baroclinic instabilities (Bachman and Fox-Kemper, 2013; Boccaletti et al., 2007; Brüggemann and Eden, 2014; Mahadevan et al., 2010; Nurser and Zhang, 2000; Samelson, 1993; Skyllingstad and Samelson, 2012) amongst others. While there is evidence for each of these processes affecting upper ocean stratification, the interactions between them and their relative strength over the seasonal cycle remain major outstanding questions (Belcher et al., 2012; Callies et al., 2015; Capet et al., 2008a; Hamlington et al., 2014; Haney et al., 2012; Lévy et al., 2010; Mensa et al., 2013; Taylor and Ferrari, 2010).

An important point of reference for this work is an insightful series of papers by Capet and co-authors (Capet et al., 2008a; 2008b; 2008c), that examine the transition from mesoscale to submesoscale dynamics in a model domain analogous to the California Current System. An advantage of this approach over a channel model configuration is that the submesoscale processes occur in the context of the strain induced by a larger scale eddy field. This strain may be an important control on the growth rate of instabilities (Bishop, 1993; McWilliams and Molemaker, 2011; Spall, 1997; Thomas, 2012). A comparable experimental methodology is employed in this work whereby simulations are run over a resolution range from mesoscale-resolving to submesoscale-permitting. These simulations depart from previous works in a number of ways. First, a

* Corresponding author. Tel.: +44 1865 282429.
E-mail address: brannigan@atm.ox.ac.uk (L. Brannigan).

http://dx.doi.org/10.1016/j.ocemod.2015.05.002
1463-5003/

seasonally varying surface buoyancy forcing is employed and so the mean mixed layer depth varies by an order of magnitude through the year. Second, no temperature-restoring is used and so the model stratification can diverge as the resolution becomes finer. Third, the domain used here is analogous to an open ocean region rather than an eastern boundary current region (Capet et al., 2008a; 2008b; 2008c) or a western boundary current region (Gula et al., 2014; Mensa et al., 2013).

This experiment is carried out in an idealised configuration intended to be analogous to the OSMOSIS (Ocean Surface Mixing - Ocean Submesoscale Interaction Study) observation site in the North Atlantic. The observation site is the Porcupine Abyssal Plain located near (16°W, 49°N) a region where mean flows are weak and mesoscale eddies dominate the kinetic energy budget (Painter et al., 2010). This numerical experiment complements a moored array of instruments, seaglider deployments and two process cruises in the project. Comparisons will be made to these observations as the results are presented, though we note the model has not been 'tuned' to replicate the observations.

This paper is structured as follows. The experimental set-up is given in Section 2. The structure of the buoyancy and velocity fields and the balance relationships that connect them are shown in Section 4. The magnitude of the different submesoscale processes across the seasonal cycle in Section 4. A summary and discussion of the implications for efforts to observe and parameterise submesoscale flows follow in Section 5.

2. Experimental set-up

2.1. Model domain

The simulations are integrated using the MITgcm (Marshall et al., 1997) in a hydrostatic configuration. The model set-up is analogous to the OSMOSIS observation area at the Porcupine Abyssal Plain site. As such, the configuration is that of an open ocean location in the mid-latitudes where the kinetic energy budget is dominated by mesoscale eddies. The domain is doubly-periodic with side-length of 256 km. The bottom boundary is at 3700 m depth and the model domain is spanned with 200 vertical levels. The vertical grid-spacing is reduced near the top and bottom boundaries to 3 m to better resolve the boundary layer processes of interest and increases gradually to a maximum of 32.5 m in the interior.

A series of simulations are carried out with uniform horizontal grid resolutions of 4 km, 2 km, 1 km and 0.5 km. The 4 km run acts as the control for our experiment, though comparisons are also made with observations to ensure the model state is a reasonable representation of the real ocean. The simulations are run on the UK ARCHER supercomputer, a Cray XC30 system. All of the runs are integrated for at least five years with the fifth year used to perform the analysis.

2.2. Numerical configuration

A linear equation of state in temperature is employed with a thermal expansion coefficient $\alpha = 2 \times 10^{-4}$ K^{-1} and so $b = g\alpha(T - T_{ref})$ where b is buoyancy, $g = 9.81$ m s^{-2} is gravity, T is temperature and T_{ref} is a reference temperature. Simulations of geostrophic turbulence generate a downscale cascade of enstrophy that must be dissipated to prevent it accumulating at the grid-scale. Enstrophy is dissipated in the momentum equation using adaptive viscous schemes first developed by Smagorinsky (1963), Leith (1996) and Fox-Kemper and Menemenlis (2013). Recent results show that adaptive viscous schemes are necessary to allow submesoscale turbulence to develop (Graham and Ringler, 2013; Ilicak et al., 2012; Ramachandran et al., 2013). Diffusion is applied to horizontal gradients in temperature. For both horizontal diffusion and viscosity, biharmonic operators are chosen over Laplacian operators so that explicit diffusion and viscosity are targeted at the highest wavenumbers (e.g. Griffies and Hallberg, 2000; Graham and Ringler, 2013). At all resolutions the Smagorinsky coefficient is 3, while the Leith and modified Leith coefficients are 1. The biharmonic temperature diffusion coefficient is 4×10^7 m^4 s^{-1} at 4 km resolution and reduced by a factor of four for each doubling in resolution. A partial-slip bottom boundary condition is imposed with a quadratic bottom drag (Arbic and Scott, 2008) using a non-dimensional quadratic drag coefficient of 3×10^{-3}.

In addition, vertical mixing of both heat and momentum is carried out with a Laplacian operator with a constant diffusion coefficient of 4×10^{-5} m^2 s^{-1}. The mixed layer depth is defined throughout as the first depth where the temperature difference from the surface is greater than 0.1 °C.

The advection of temperature is carried out using the Prather scheme (Prather, 1986). This is an upwind scheme that conserves second-order moments in sub-grid tracer distributions and so helps to preserve the sharp frontal structures of interest. Hill et al. (2012) show that the effective diffusivity of the Prather scheme is similar to the level of diffusion estimated for the real ocean by tracer release studies. The model's default second-order centered advection scheme is employed for momentum.

The timestep is 400 s at 4 km resolution and is then reduced by a factor of two with each doubling in resolution. The model is integrated on an f-plane with a Coriolis frequency $f = 10^{-4}$ s^{-1}. Note that no temperature relaxation conditions are employed and so the model solution can evolve freely.

2.3. Boundary layer parameterisation

In the vertical, the model is run with the K-profile parameterisation (*KPP*, Large et al., 1994) for the surface boundary layer. This scheme is in practice a suite of parameterisations that aim to represent a number of mixed layer processes. The *KPP* scheme increases the vertical viscous/diffusive coefficients (hereafter 'diffusive coefficients') based on the surface wind stress. It also increases the diffusive coefficients if there is elevated shear at the base of the mixed layer based on a Richardson number criteria. In the event of destabilising surface buoyancy forcing the *KPP* scheme introduces a vertical non-local transport to capture the effect of vertical convective mixing (Marshall and Schott, 1999). The *KPP* scheme also applies higher diffusive coefficients in the event of negative stratification, even if this is not associated with destabilising surface buoyancy forcing as can occur in the presence of down-front winds. In these cases of static instability the *KPP* scheme applies a high (5×10^{-3} m^2 s^{-1}) vertical diffusion coefficient rather than instantaneously mixing buoyancy as done by the default MITgcm convective adjustment scheme or the Price et al. (1986) scheme.

2.4. Initial and boundary conditions

The model is initialised at rest with a horizontally uniform temperature profile. The initial vertical temperature profile (Fig. 1, left panel) is derived from an Argo float near the Porcupine Abyssal Plain observation site. This profile was sampled on 23rd March 2012 and is selected as a temperature profile with minimal signs of internal wave heaving or instrument noise.

The model is forced at the surface by a heat flux and wind forcing. The prescribed heat flux is uniform across the domain and averages to zero over each 360-day year (Fig. 1, right panel) with values based on the sum of the net shortwave, longwave, sensible and latent heat fluxes from the monthly climatology of Berry and Kent (2009) for the Porcupine Abyssal Plain observation region. These heat fluxes are applied to the uppermost model level. As such, heating fluxes result in a more rapid restratification than in the real ocean where shortwave radiative fluxes penetrate in an exponentially decaying manner

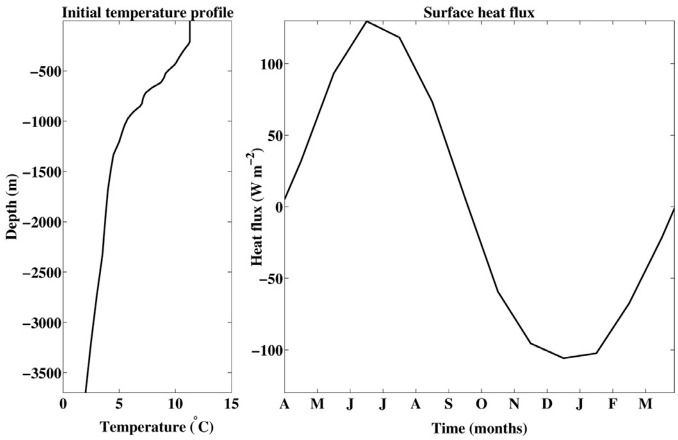

Fig. 1. (Left panel) The initial temperature profile for all simulations. (Right panel) The heat flux into the domain through the year. The model 'summer' is the first half of the year and the model 'winter' is the second half.

through the water column. The experiment aims to understand the response of mixed layer dynamics to the seasonal cycle in buoyancy forcing. Higher frequency variability, including diurnal effects, are not included in the main experiments described here.

References are made to 'summer' and 'winter' as shorthand for the periods of heating and cooling respectively. The model integration begins with stratification derived from late March conditions – as such the heating period is the first half of every model year and the cooling period is the second half. To aid readability and comparisons with observations from the real ocean, the model outputs are equated with the month they correspond to from the buoyancy forcing.

While the surface heat flux creates an annual cycle in stratification and mixed layer depth, the wind forcing produces a field of geostrophic turbulence and an Ekman transport in the near-surface. The forcing scheme used is based on that of Koszalka et al. (2009) with a streamfunction (ψ) to generate the wind stress that varies in space and time. The consequent curl of the wind stress causes isopycnals to tilt locally through Ekman pumping or suction. The velocity field undergoes Rossby adjustment to the tilt of the isopycnals and the non-linear eddy interactions then induce a turbulent eddy field.

The streamfunction is constructed using zonal and meridional Fourier modes, an example of which can be seen in Fig. 2. Unlike Koszalka et al. (2009), where a random component to each streamfunction is introduced in Fourier space, a random phase is added onto each streamfunction component-pair in order to randomise the spatial structure of the forcing from month to month with

$$\psi = \psi_0 \sum_{k,l=1}^{3} \sin\left(kx + \phi_1(k,l)\right) \sin\left(ly + \phi_2(k,l)\right), \tag{2.1}$$

where $\psi_0 = 0.02$ N m^{-1}, x and y are the zonal and meridional coordinates respectively, k and l are the zonal and meridional domain wavenumbers respectively, and ϕ_i is a random phase. A new streamfunction is generated each month and the model linearly interpolates between the successive streamfunctions to give a wind field that varies smoothly in time. Inspection of the results show this gives rise to a small amplitude monthly cycle that is not readily apparent in the key model outputs in the presence of the generally turbulent flow. The streamfunction for wind forcing is produced for the 4 km run and then interpolated to the finer resolution grids.

In addition, a constant zonal wind of 0.05 N m^{-2} is added to ensure the mixed layer depth extends beyond the uppermost model level during periods of stabilising heat forcing such that the vector wind stress $\tau = 0.05\mathbf{i} + \mathbf{k} \times \nabla\psi$ where $\mathbf{i}$ is the zonal unit vector and $\mathbf{k}$ is the vertical unit vector. The constant zonal wind is about five times larger than the root-mean-square magnitude of the spatially-

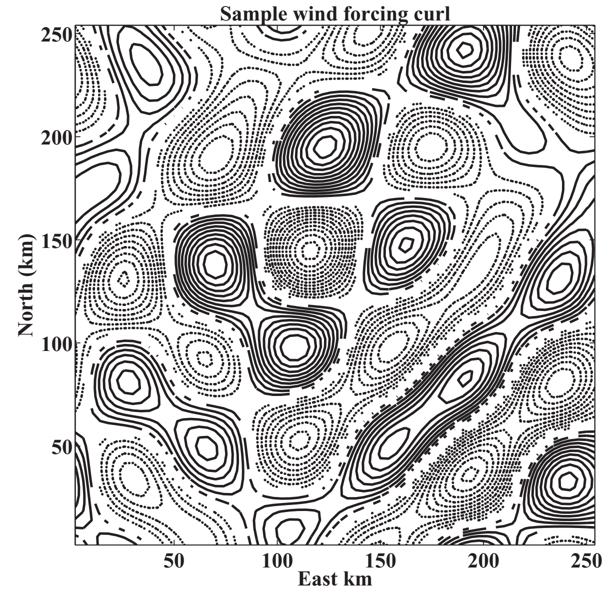

Fig. 2. A snapshot of the wind-forcing used in the model for one month, presented as the curl of the streamfunction. Solid lines are positive contours and dotted lines are negative contours with intervals of 10^{-7} m s^{-2}.

varying wind derived from the streamfunction in Eq. (2.1), and so it is the main driver of the Ekman transport.

The wind forcing has length scales of 20–256 km and so is shorter than the atmospheric length scales with the greatest energy in the mid-latitudes (Nastrom and Gage, 1985). However, the length scales of the forcing are still comparable to the baroclinic deformation radius of approximately 40 km. A test experiment has been carried out with a wind streamfunction that was constant in time. Analysis of this run after one year showed no imprint of the wind-forcing in the model output. This provides confidence that the non-linear dynamics of the eddy field dominate the solution, rather than the detailed structure of the wind forcing. The wind forcing in this experiment is continuous, but weak, with a magnitude about one-third of the root-mean-square wind stress magnitude estimated from the ERA-interim re-analysis for the region.

2.5. Averaging operator

The averaging operator denoted by an overbar is a horizontal average over a model level

$$\overline{g(\mathbf{x}, t)} = \frac{1}{A} \int_x \int_y g dx dy, \tag{2.2}$$

where g is an arbitrary function, $\mathbf{x}$ is the position vector, t is time and A is the horizontal area.

3. Results

The overall buoyancy and momentum fields are compared at different resolutions in the spin-up phase and throughout the seasonal cycle.

3.1. Spin-up and inter-annual variability

At the outset of the runs, the solutions are similar across the range of resolutions (Fig. 3, all panels). The solutions begin to diverge between resolutions after about 120 days both in terms of the standard deviation of sea surface temperature (SST), the mean mixed layer depth and the mean kinetic energy at the surface (Fig. 3, upper three

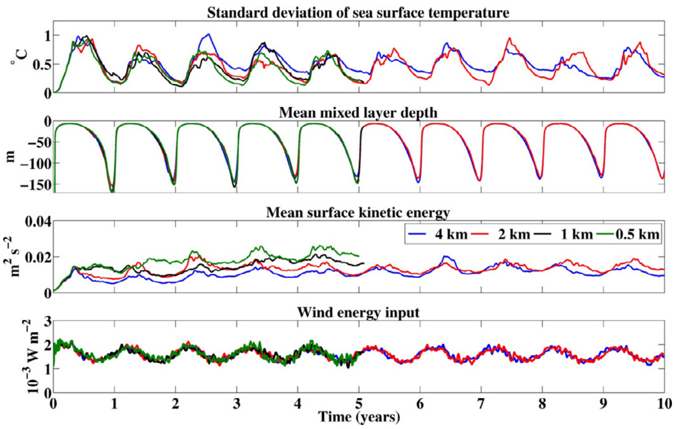

Fig. 3. Model fields during spin-up. (Top row) Standard deviation of sea surface temperature. (Second row) The mean mixed layer depth. (Third row) Mean kinetic energy at the surface. (Bottom row) The mean input of kinetic energy by the wind stress $\boldsymbol{\tau} \cdot \mathbf{u}$. The two coarser resolution simulations have been run for a further five years to Year 10.

panels). The mean energy input from the wind is similar at all resolutions (Fig. 3, bottom panel). The wind energy input is similar across resolutions despite the higher surface kinetic energy at finer resolution as the largest kinetic energy is found in the mesoscale vortices, where the wind is aligned with the flow on one side of the vortex but opposed to the flow on the other side, and so the energy input largely cancels out. From the third year of the simulations the differences between the years are in the range of year-to-year variability (Fig. 3, upper three panels). Fields with greater inter-annual variability are noted in the results below.

3.2. Vertical and horizontal buoyancy distributions

Level mean vertical temperature profiles ($\overline{T}$) at the end of the heating and cooling period are shown in Fig. 4 below. These profiles show that at finer resolution there is a cooler and deeper mixed layer (Fig. 3, second row) and this is found in both summer and winter. The dynamical causes of this will be explored further in a subsequent manuscript. The difference in $\overline{T}$ between the runs falls to zero by 350 m depth. The range of mixed layer depths from approximately 0 m to 250 m in the model is similar to those estimated over the seasonal cycle from seaglider observations at the Porcupine Abyssal Plain site (Damerell et al., in prep. for Geophys.Res.Lett.).

Qualitative differences in the horizontal distribution of buoyancy are illustrated in the snapshots of the magnitude of buoyancy gradients at the sea surface in Fig. 5. These snapshots are from January of the fifth year of the simulations, when the mean mixed layer depth is approximately 90 m. Fig. 5 shows that fronts become stronger, sharper and more sinuous as the resolution is made finer. In contrast to Capet et al. (2008a), filamentary submesoscale features are also present inside the large vortices, for example in the anti-cyclone at (50 km, 50 km) in the lower-right panel of Fig. 5. This filamentation occurs whenever the mixed layer is deeper than approximately 40 m at the finest resolution.

Values of $\overline{|\nabla_h b|}$, the level-mean magnitude of the horizontal buoyancy gradient, where ∇_h is the horizontal gradient operator, are shown in Fig. 6. The root-mean-square magnitude of these gradients is $O(10^{-7}\ s^{-2})$, with the largest values an order of magnitude stronger, typical of those observed in the mid-latitude mixed layer (e.g. Hosegood et al., 2006). There is an increase in $\overline{|\nabla_h b|}$ as the resolution is made finer, as previously noted by Capet et al. (2008a). At the start of the heating period – for example in May in Fig. 6 – the mean gradients are low at all resolutions. As the heating period progresses $\overline{|\nabla_h b|}$ increases more quickly as the resolution is made finer, for example in July in Fig. 6. It then decreases more rapidly at finer resolution in the cooling period as the mixed layer begins to deepen. We note that there is significant variation in the values of $\overline{|\nabla_h b|}$ from year-to-year, though the annual cycle persists. The seasonal cycle in horizontal buoyancy gradients found here agrees with glider observations from the Porcupine Abyssal Plain site. Alternative model forcings that include a diurnal cycle in heating and stronger wind forcing have been carried out at 2 km resolution. The results of these experiments have a similar seasonal cycle of horizontal buoyancy gradients.

While $\overline{|\nabla_h b|}$ captures variability at the grid scale, the horizontal distribution of buoyancy over the whole surface level can be considered using the power spectral density (PSD) of SST. The spectra are calculated in horizontal wavenumber shells after the application of a 2D Hanning window. As for Capet et al. (2008c) the spectra are multiplied by four to recover the variance from before the windowing operation. Fig. 7 shows the spectra averaged over April–September (left panel) and October–March (right panel). There is an increase in variability at shorter wavelengths as the resolution is made finer, previously found by Capet et al. (2008a). A comparison of the upper

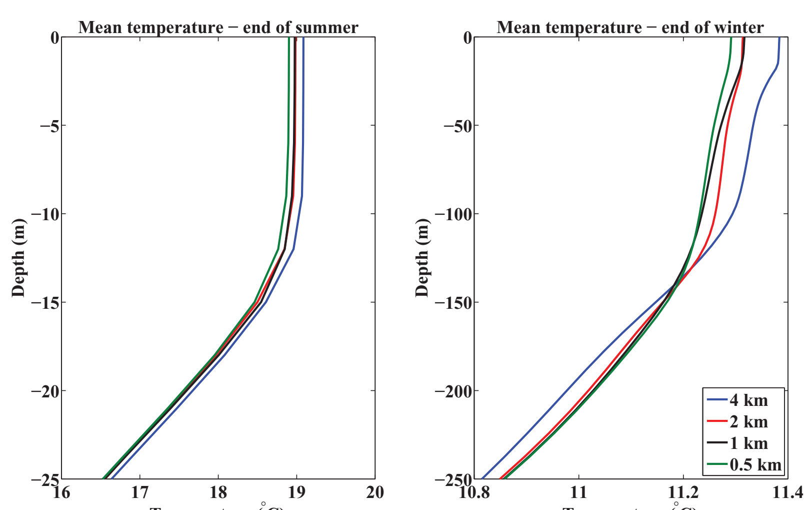

Fig. 4. Mean temperature profiles. (Left panel) The temperature profile at the end of summer in the fifth model year. (Right panel) The temperature profile at the end of winter in the fifth model year. Note the different scales between the panels on both axes.

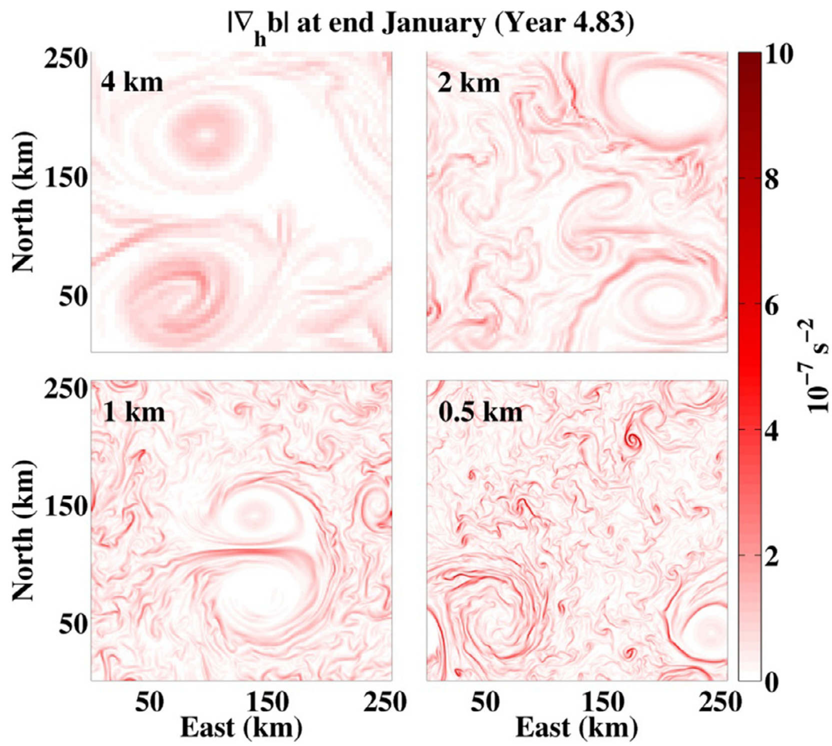

Fig. 5. A snapshot of the magnitude of the sea surface buoyancy gradient at the indicated grid resolutions. The snapshots are derived from the model state in late January (year 4.83) when the mean mixed layer is approximately 90 m deep. The surface relative vorticity at this time point is shown in Fig. 10.

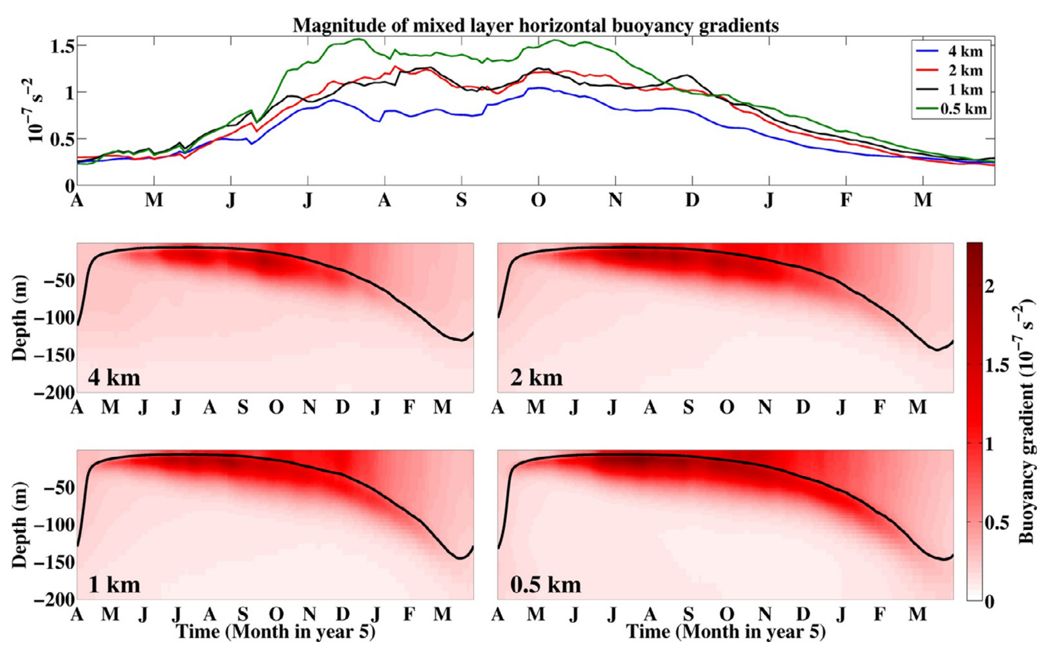

Fig. 6. The mean horizontal buoyancy gradient $\overline{|\nabla_h b|}$ over the fifth year of the simulations at 2-day intervals. (Upper panel) The mean horizontal buoyancy gradient in the mixed layer. (Lower panels) The vertical profile of $\overline{|\nabla_h b|}$. The black line in the lower panels shows the mean mixed layer depth at that time.

panels in Fig. 7 shows that there is a shallowing of the spectral slope from summer to winter.

3.3. Velocity field

The root-mean-square velocities are about 15 cm s^{-1} at fine resolution, that is about 30% less than those observed at the observation site (Painter et al., 2010). The mean flow in the model is an Ekman spiral driven by the zonal mean wind stress (not shown).

The slopes of the power spectral density of surface velocity are similar to those for SST anomalies with the slope shallowing from near −3 in summer (Fig. 8, upper-left panel) to approximately −2 as the winter progresses (Fig. 8, upper-right panel). The slope is evaluated quantitatively by performing a linear regression on the power spectral density in log–log space at each resolution over the annual

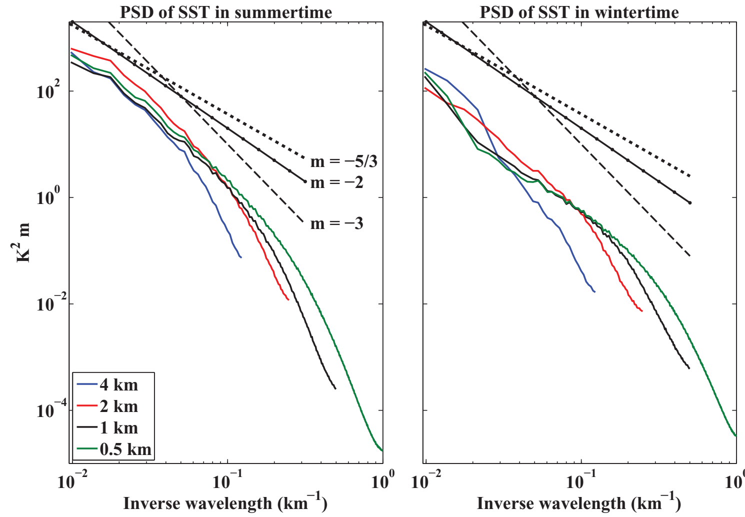

Fig. 7. The power spectral density of sea surface temperature. (Left panel) The horizontal spectra averaged over the heating period. (Right panel) The horizontal spectra averaged over the cooling period. The dotted lines show reference slopes *m* in log–log space.

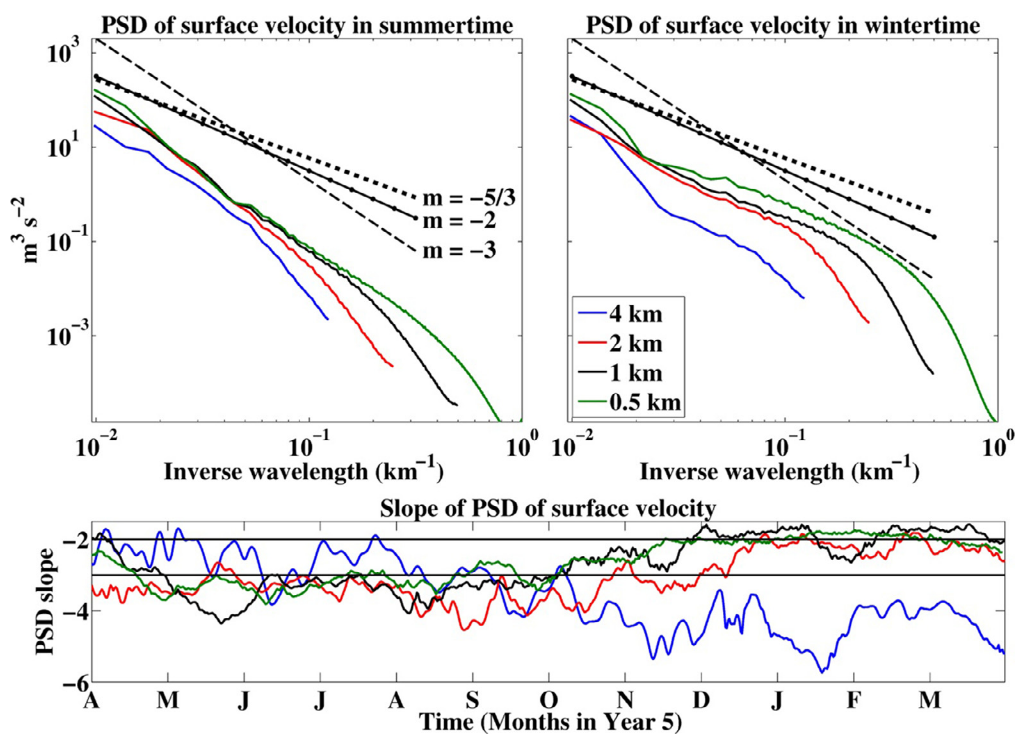

Fig. 8. The power spectral density for surface velocity. (Upper-left panel) The power spectral density averaged over the heating period (April–September). (Upper-right panel) The power spectral density averaged over the cooling period (October–March). The dotted lines show reference slopes *m* in log–log space. (Lower panel) Time series of the regressed spectral slopes. The reference horizontal lines in the lower panel are at 2 and −3. The upper-limit on the *y*-axis is a slope of 5/3.

cycle. To reduce domain-scale and grid-scale effects, this regression is carried out over the range of wavelengths from four times the grid spacing for each simulation to 100 km. The regressed slope remains merely an estimate of the change in the spectral slope due to increasing curvature in the slope in winter. The time series of regressed slopes in Fig. 8 (lower panel) shows that the slope quickly steepens to values between −4 and −3 in the restratification period (April–May). The slope remains relatively steep until the cooling begins in September, at which point the slope starts shallowing until reaching a value between −5/3 and −2 in December when the mixed layer has reached approximately 40 m depth. The slope then stops shallowing even as the mixed layer continues to deepen to 150 m in March. These seasonal variations in slopes are consistent with observations of the North Atlantic (Callies et al., 2015) and numerical simulations of the North Atlantic that resolve basin-scale features (Lévy et al., 2010; Mensa et al., 2013). We note that the steeper slopes in summer could also be due to the mixed layer deformation radius with shallow mixed layers being less than the model grid resolution. The seasonal cycle in the slope shown in Fig. 8 (lower panel) occurs consistently from year-to-year in the three finer resolution cases. The coarsest resolution case is more variable, but the same overall cycle emerges if a multi-year average of the cycle is taken.

Fig. 9 (left panel) shows the vertical profile of the power spectral density of the horizontal velocity in January at the finest resolution. The plot is a colour equivalent of the spectra in Fig. 8 (upper panels). Shallower spectral slopes are found where the light colours extend to shorter wavelengths. Fig. 9 (right panel) shows the same regression slopes as Fig. 8 (lower panel), but applied in the vertical. The

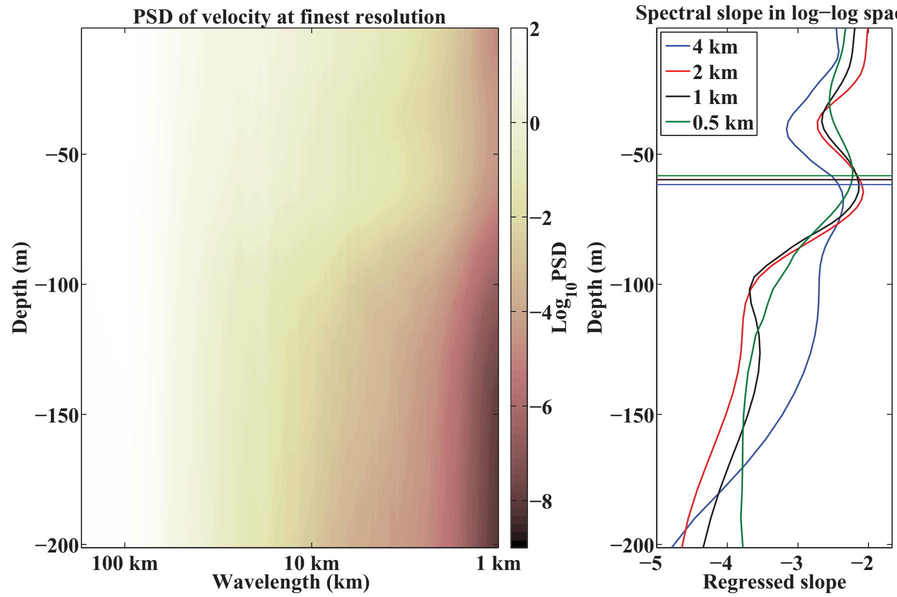

Fig. 9. The vertical structure of the power spectral density of velocity in early January during the cooling phase. (Left panel) A colour plot of the PSD at fine resolution. (Right panel) The spectral slope for all resolutions as estimated from a linear regression in log–log space. The coloured horizontal lines show the mean mixed layer depth at the corresponding resolution.

regime of shallow spectral slopes is confined to the mixed layer at all resolutions, the mean depth of which is marked by a horizontal line of the same colour. We note that the transition from shallow to steep slopes happens near the mean mixed layer depth of 60 m in Fig. 9, and so is not related to the increase in vertical grid spacing that begins from 90 m depth at all resolutions. These vertical profiles of spectral slopes are consistent with the mixed layer being better approximated by quasi-geostrophic dynamics with a vertical scale of the mixed layer depth rather than surface quasi-geostrophy (sQG), as in the latter case shallower spectral slopes are also expected below the mixed layer (Callies and Ferrari, 2013).

The implications of the seasonal cycle in the power spectral density of surface velocity at the different resolutions is apparent in relative vorticity at the surface through the year. The animation provided as a supplementary material shows that the steep spectral slopes in summer correspond to the vertical component of relative vorticity dominated by the largest mesoscale vortices. As the cooling begins from September, more submesoscale features in relative vorticity emerge in frontal regions and inside the anti-cyclonic eddies. As the winter progresses these come to occupy the entire domain, as shown in Fig. 10.

3.4. Momentum balance

The various balances of momentum give an understanding of how the dynamics differ across resolutions and through the seasonal cycle. Following Capet et al. (2008b), a metric for geostrophic balance is

$$\epsilon_{geo}(\mathbf{x},t) = 1 - \frac{|f\zeta_z - \frac{1}{\rho}\nabla_h^2 p|}{f|\zeta_z| + |\frac{1}{\rho}\nabla_h^2 p| + \mu_{geo}}, \tag{3.1}$$

where $\zeta_z = v_x - u_y$ is the vertical component of relative vorticity, p is pressure and $\mu_{geo} = f\zeta_{z,\mathrm{RMS}} + \rho^{-1}\nabla_h^2 p_{\mathrm{RMS}}$ is a small constant included to avoid spurious large values in areas of weak force balance. Note that the scale has been reversed from Capet et al. (2008b) such that $\epsilon_{geo} = 1$ means full geostrophic balance.

Capet et al. (2008b) also investigate a generalised cyclostrophic or gradient-wind balance that includes the full non-linear advective terms

$$\epsilon_{adv}(\mathbf{x},t) = 1 - \frac{|f\zeta_z + \nabla_h\cdot(\mathbf{u}\nabla\mathbf{u}_h) - \frac{1}{\rho}\nabla_h^2 p|}{f|\zeta_z| + |\nabla_h\cdot(\mathbf{u}\nabla\mathbf{u}_h)| + |\frac{1}{\rho}\nabla^2 p| + \mu_{adv}}, \tag{3.2}$$

where $\mathbf{u} = (u, v, w)$ is the velocity vector and μ_{adv} is adapted from μ_{geo} to include the contribution of the advective terms. A similar notation is adopted for this term in the balances below. The advection terms include the centripetal acceleration and so this non-linear balance may better describe the force balance in vortices and at curved fronts.

The model solution also supports internal waves that lead to more rapid accelerations than those associated with the geostrophic flow. Although the inclusion of the time derivative means the momentum is no longer ‘balanced’, the inclusion of the time derivative provides useful insight, as discussed below. This ‘balance’ is called a ‘time-advection’ balance by including the divergence of the time derivative of the horizontal velocities

$$\epsilon_{time-adv}(\mathbf{x},t) = 1 - \frac{|f\zeta_z + \nabla_h\cdot\mathbf{u}_{h,t} + \nabla_h\cdot(\mathbf{u}\nabla\mathbf{u}_h) - \frac{1}{\rho}\nabla_h^2 p|}{f|\zeta_z| + |\nabla_h\cdot\mathbf{u}_{h,t}| + |\nabla_h\cdot(\mathbf{u}\nabla\mathbf{u}_h)| + |\frac{1}{\rho}\nabla_h^2 p| + \mu_{time-adv}}, \tag{3.3}$$

where the subscript t denotes differentiation in time.

In a simulation of filamentogenesis in the Gulf Stream Gula et al. (2014) find that the vertical viscous fluxes are of the same order as the vertical shear and horizontal buoyancy gradient in thermal wind balance. They term this ‘turbulent thermal wind balance’. This is quantified here as a ‘turbulent geostrophic balance’ by modifying (3.1) as

$$\epsilon_{tg}(\mathbf{x},t) = 1 - \frac{|f\zeta_z + \nabla_h\cdot(\tau_z) + \nabla\cdot((K\mathbf{u}_z)_z) - \frac{1}{\rho}\nabla_h^2 p|}{f|\zeta_z| + |\nabla_h\cdot(\tau_z)| + |\nabla_h\cdot((K\mathbf{u}_z)_z)| + |\frac{1}{\rho}\nabla_h^2 p| + \mu_{tg}}, \tag{3.4}$$

where K is the vertical viscous coefficient that is set by the *KPP* scheme in the mixing layer but is a constant below and τ_z is the wind stress divergence that accelerates the flow in the uppermost level. This is thus also a generalised version of the ‘turbulent Ekman balance’ of Taylor and Ferrari (2010).

Finally, to ascertain whether a full description of balance is being approached we can combine all of the terms from the turbulent and

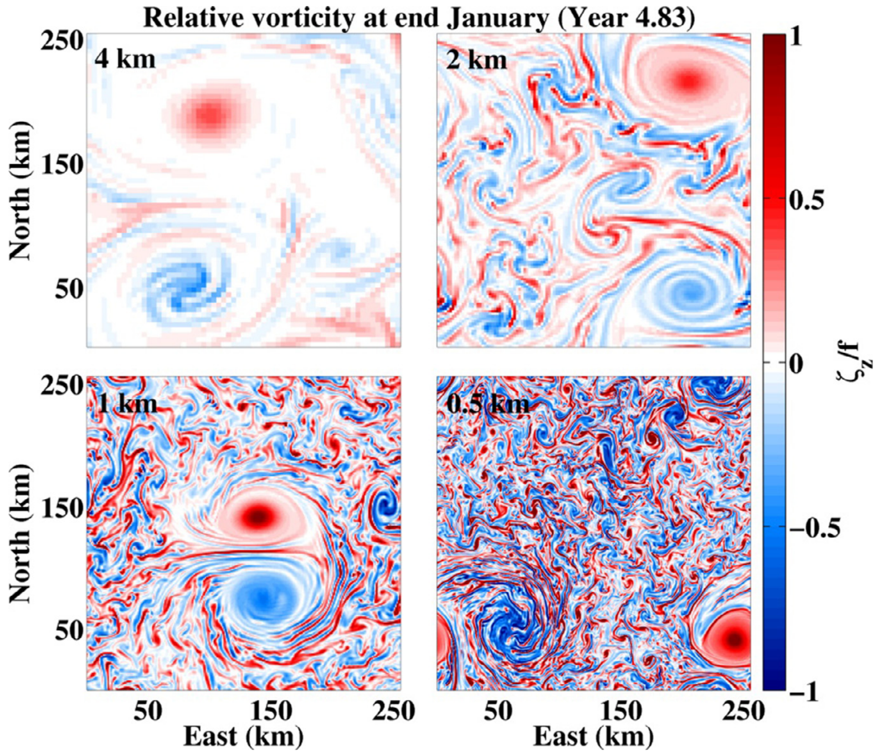

Fig. 10. A snapshot of the vertical component of relative vorticity at the surface. The panels are at the indicated grid resolutions, though the labels are somewhat obscured in the lower panels. As for Fig. 5, the snapshots are derived from the model state in late January (year 4.83) when the mean mixed layer is approximately 90 m deep.

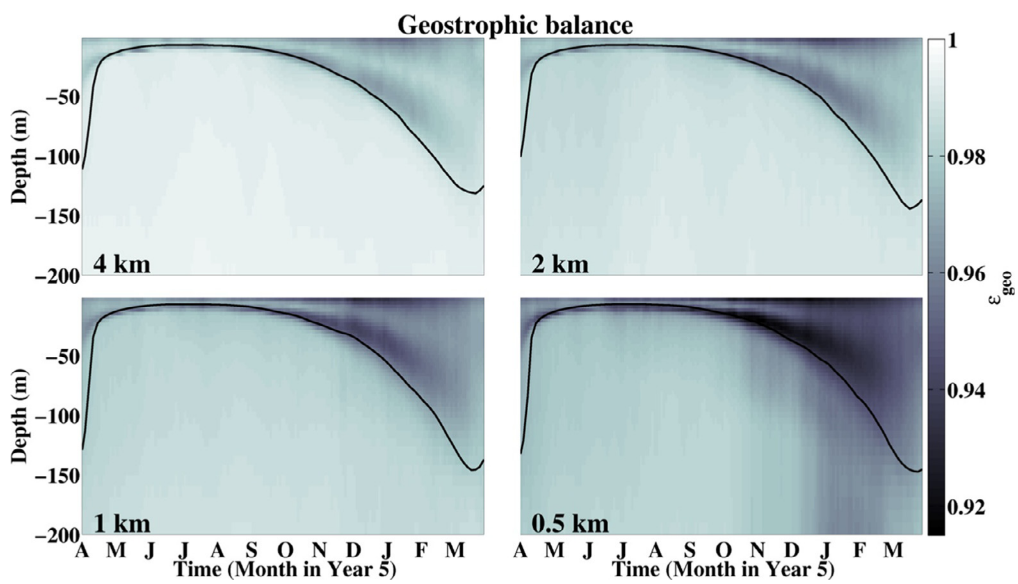

Fig. 11. The degree of geostrophic balance $\overline{\epsilon_{geo}}$ calculated from snapshots of model output at 2-day intervals through the seasonal cycle. Darker colours indicate a departure from geostrophic balance. The black line is the mean mixed layer depth.

time-advection balances as

$$\epsilon_{tta}(\mathbf{x},t) = 1 - \frac{|f\zeta_z + \nabla_h\cdot(\tau_z) + \nabla_h\cdot((K\mathbf{u}_z)_z) + \nabla_h\cdot\mathbf{u}_t + \nabla_h\cdot(\mathbf{u}\nabla_h\mathbf{u}) - \frac{1}{\rho}\nabla_h^2 p|}{f|\zeta_z| + |\nabla_h\cdot\mathbf{u}_t| + |\nabla_h\cdot((K\mathbf{u}_z)_z)| + |\nabla_h\cdot(\mathbf{u}\nabla_h\mathbf{u})| + |\frac{1}{\rho}\nabla_h^2 p| + \mu_{tta}}. \tag{3.5}$$

The annual cycle in $\overline{\epsilon_{geo}}$ is shown in Fig. 11. This shows that the degree of geostrophic balance falls as the resolution is made finer, both in the mixed layer and in the interior. Vertically, the degree of balance is lower in the mixed layer than in the interior, though minima are often found at the base of the deepening mixed layer.

While geostrophic balance is the primary balance, there is a change in the residual mean balance across this range of resolutions. Fig. 12 shows the vertical profiles of the horizontal mean of the various balances in late January, when the mean mixed layer depth is approximately 90 m. This is during the time interval when $\overline{\epsilon_{geo}}$ is relatively low in the thermocline of the finest resolution case (Fig. 11, bottom-right panel). Comparing firstly the geostrophic balance, Fig. 12 (top-left panel) shows again that the magnitude of $\overline{\epsilon_{geo}}$ falls as the resolution is made finer. Moving to the turbulent geostrophic balance (Fig. 12, top-right panel) improves the degree of balance over geostrophy alone. However, this improvement in balance is only in the mixed

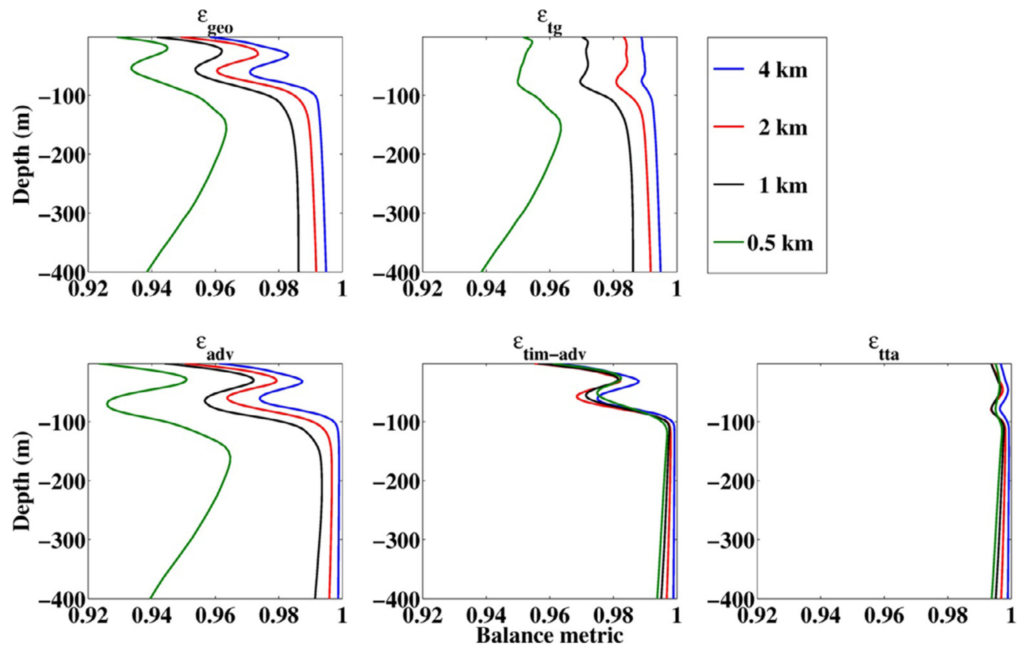

Fig. 12. Vertical profiles of the balance parameters (x-axis in all panels) in late January (year 4.83) during the period of mixed layer deepening. The mean mixed layer is approximately 90 m at all resolutions. The calculation is based on a snapshot of model output. (Top left) Geostrophic balance as measured by $\overline{\epsilon_{geo}}$. (Top centre) Turbulent geostrophic balance as measured by $\overline{\epsilon_{tg}}$. (Bottom left) Advective balance as measured by $\overline{\epsilon_{adv}}$. (Bottom centre) Time-advective balance as measured by $\overline{\epsilon_{time-adv}}$. (Bottom right) Turbulent-linear-cyclostrophic balance as measured by $\overline{\epsilon_{tta}}$.

layer, as the vertical diffusion of momentum in the interior is much weaker. Now comparing geostrophy and the advective balance ϵ_{adv}, Fig. 12 (left-hand panels) shows that incorporating advective terms improves the degree of balance by a small amount at coarser resolution. However, for the two finer resolutions the advective balance is actually slightly less than the geostrophic balance near the base of the mean mixed layer at 90 m and the degree of balance does not materially improve with the advective balance in the thermocline. In order to better describe the momentum 'balance' at the finest resolution, the time derivative terms must be included (centre panel, bottom row). In the coarser resolution runs, the addition of the time derivative term makes little difference and $\overline{\epsilon_{adv}} \approx \overline{\epsilon_{time-adv}}$. Therefore, the time derivative terms become an important part of the residual momentum balance in late winter at finer resolution in the mixed layer and thermocline. The combined balance terms in $\overline{\epsilon_{tta}}$ are shown in Fig. 12 (right panel, bottom row), with the residual accounted for by the horizontal diffusion of momentum in the mixed layer and a small factor due to the time-stepping scheme.

A physical sense for the change in the residual balance across resolutions can be gained by considering the geostrophic balance ϵ_{geo} at the base of the mixed layer in Fig. 13. This is taken from the same time as the sea surface buoyancy gradients plot in Fig. 5 and the mean balances in Fig. 12. The advective and time derivative terms account for the departure from balance near (60 km, 60 km) in Fig. 13 (bottom-right panel) and are thus associated with the long filamentary streaks that are wrapped into the large anti-cyclone there and visible as buoyancy gradients in Fig. 5. As such the filaments are indicative of an unbalanced process that is developing rapidly in time. The dynamical process that generates these filaments is considered in more detail in a forthcoming paper (Brannigan, in prep.). Such filamentation and the accompanying departure from geostrophic balance becomes weaker as the resolution becomes coarser (Fig. 13). Lower values of ϵ_{geo} are increasingly found in the large vortices at all resolutions as the resolution is made finer. It is here that the degree of balance is most improved by moving to advective balance ϵ_{geo} that includes the centripetal acceleration and so the mixed layer portion of the mesoscale vortices becomes more non-linear as the resolution is made finer. The improvement in balance in the mixed layer by the use of turbulent geostrophic balance, measured by ϵ_{tg}, is relatively uniform through the domain (not shown).

4. Frontal processes

The results in Section 3 show that there are distinct differences across the resolutions in terms of the buoyancy, velocity and balances and growing seasonal differences between the runs. These differences are due to submesoscale processes, that are diagnosed individually here.

4.1. Frontogenesis

Although frontogenesis is formally defined to be the development of a discontinuity in buoyancy at a front, it is taken here to mean the action by the flow field to increase or decrease the variance of horizontal buoyancy gradients. The impact of frontogenesis on horizontal gradients is diagnosed using the frontogenesis function (Hoskins and Bretherton, 1972) modified to include the vertical advective transport

$$F_s = \mathbf{Q}_s \cdot \nabla_h b, \tag{4.1}$$

where:

$$\mathbf{Q}_s = -(u_x b_x + v_x b_y + w_x b_z, u_y b_x + v_y b_y + w_y b_z). \tag{4.2}$$

In agreement with Capet et al. (2008b), the mean magnitude of frontogenesis generally grows as the resolution becomes finer with level-mean values increasing by approximately a factor of two for each doubling in resolution (Fig. 14, all panels). Of more novelty is the seasonal cycle in the magnitude of frontogenesis as the mixed layer depth varies by an order of magnitude from summer to winter. Fig. 14 shows that $\overline{F_s}$ is low in the initial period of mixed layer restratification (April–June, all panels). It then grows in magnitude through the remainder of the summer and into autumn and early winter (August–December) before weakening in the late winter when the mixed layer deepens from 80 m to 150 m. The weakening of $\overline{F_s}$ in winter (all panels) could reflect the ability of mixed layer instabilities to overturn strong buoyancy gradients when the mixed layer is of sufficient

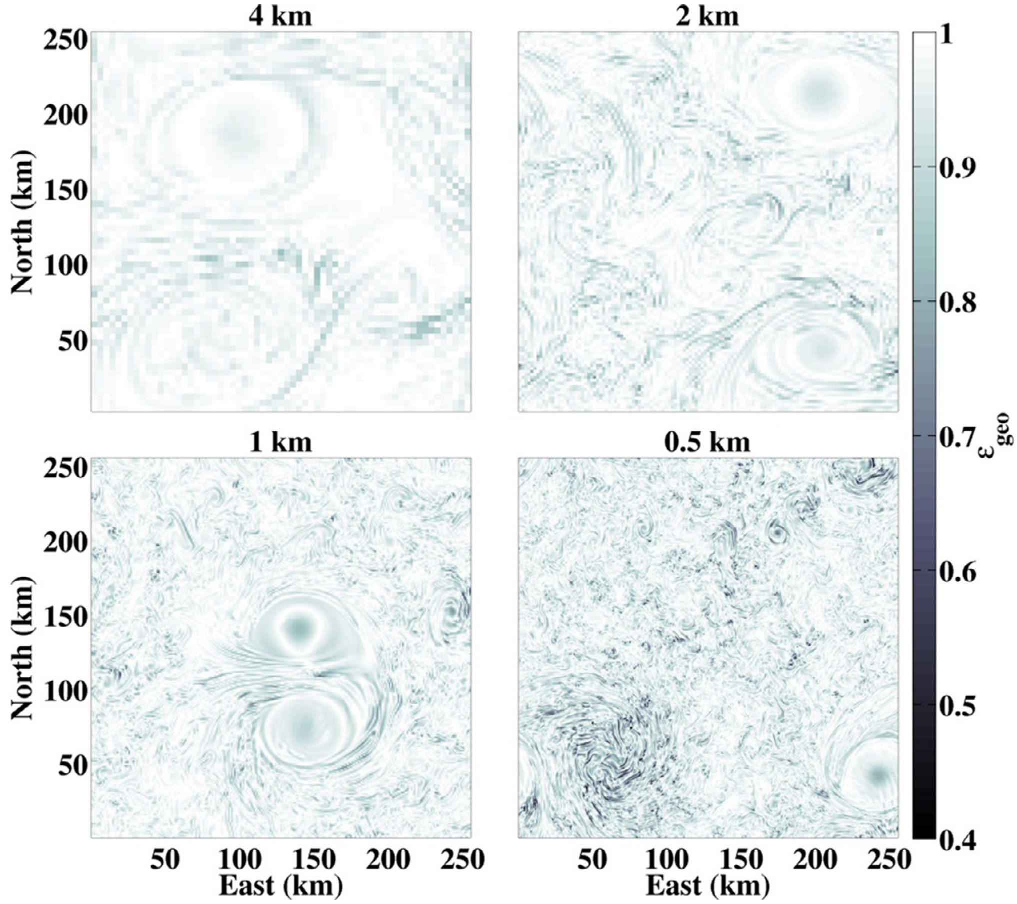

Fig. 13. Plan views of the geostrophic balance parameter ϵ_{geo} near the base of the mean mixed layer at 74 m depth in late January (at year 4.83). Darker colours show departures from geostrophic balance. This is taken from the same time as the plot of sea surface buoyancy gradients in Fig. 5 and the surface relative vorticity in Fig. 10.

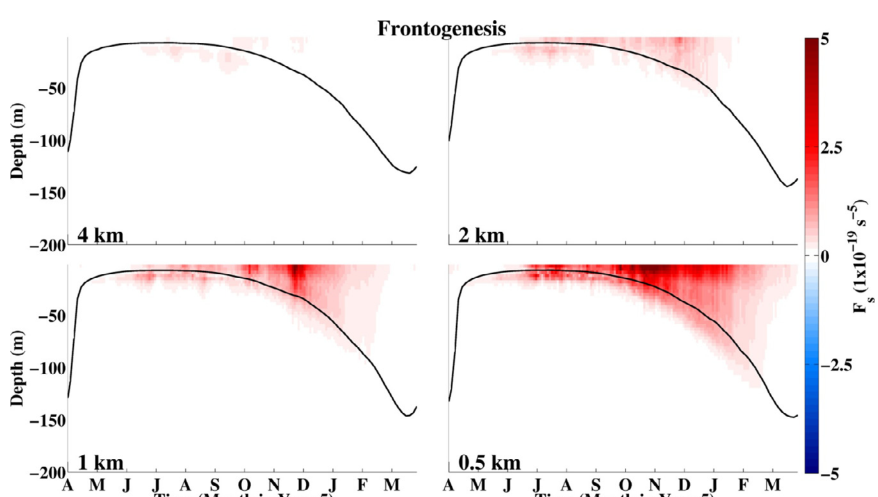

Fig. 14. The level-mean value of the frontogenesis function, defined in Eq. (4.1), by model level over the fifth year of the simulations. The calculation is based on snapshots of model output at 2-day intervals. The black line shows the mean mixed layer depth at that time.

depth. The period in the annual cycle when $\overline{\mathbf{Q}_s}$ begins to weaken coincides with the interval when the slope of the surface velocity spectra reaches its shallower values in Fig. 8 (bottom panel).

4.2. Ekman buoyancy fluxes

The creation or destruction of potential vorticity, taken to be the Ertel potential vorticity $q = (f + \nabla \times \mathbf{u}) \cdot \nabla b$, due to frictional forcing at the boundary has been established observationally and numerically as an important process at ocean fronts (Capet et al., 2008b; D'Asaro et al., 2011; Mahadevan et al., 2010; Taylor and Ferrari, 2010; Thomas, 2005). This process is referred to as the Ekman buoyancy flux (EBF) and can be diagnosed as

$$\mathrm{EBF} = \left(\frac{\tau}{\rho_0 f} \times \mathbf{k}\right) \cdot \nabla_h b, \tag{4.3}$$

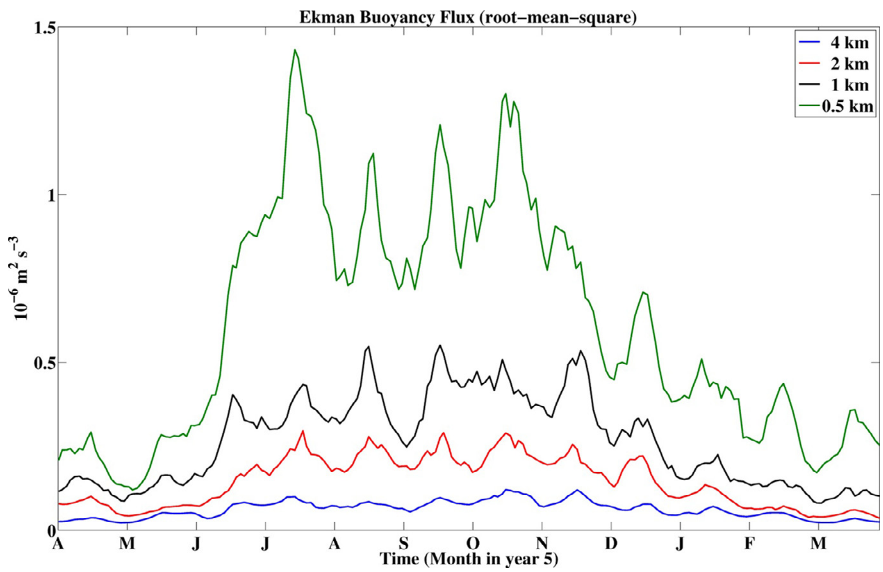

Fig. 15. The root-mean-square magnitude of the Ekman buoyancy flux, defined in Eq. 4.3, over the fifth year of the simulations.

where τ is the wind stress, ρ_o is a reference density and $\mathbf{k}$ is the unit vertical vector. The term $\nabla_h b$ is formally the mean buoyancy gradient over the Ekman layer, though we take it to be the surface buoyancy gradient. While the mean value of the EBF is notionally zero when averaged over a periodic domain, there is still a net effect on stratification as the down-front winds induce a vertical diffusive mixing through the whole mixed layer, while the up-front winds induce an advective restratification in the Ekman layer (Thomas and Ferrari, 2008). In locations of up-front winds, the Ekman layer is generally shallower than 30 m.

Fig. 15 shows that the root-mean-square Ekman buoyancy flux has a similar annual cycle to $\overline{F_s}$ in that its peak values occur in summer conditions when $\overline{|\nabla_h b|}$ is largest and it is stronger at finer resolution. The magnitude of the buoyancy fluxes is of order 10^{-6} m^2 s^{-3} at fine resolution. This is some 20 times larger than the buoyancy flux due to the peak surface heating/cooling and emphasises the local importance of the EBF in setting stratification (Thomas and Ferrari, 2008; Thomas et al., 2013) even in these simulations where the mean wind stress is moderate compared to values achieved in the open ocean. Although the winds are relatively weak here, the magnitude of the horizontal buoyancy gradients that arise are much stronger. The oscillations in the EBF in Fig. 15 are the main consequence of the monthly cycle in the wind-forcing noted in Section 2. The effect of the EBF is investigated further in Section 4.3.

4.3. Instabilities of negative potential vorticity

The ocean is subject to a range of instabilities when $fq < 0$, which in these simulations is equivalent to negative potential vorticity. Where negative potential vorticity occurs, the dominant expected response to perturbations can be inferred from the balanced Richardson number $\mathrm{Ri_b}$ (defined in Eq. (4.4)). The infinite range of possible $\mathrm{Ri_b}$ can be contracted to an angle ϕ following the approach of Thomas et al. (2013) where a schematic can be found

$$\phi_{\mathrm{Ri_b}} = \tan^{-1}(-\mathrm{Ri_b}^{-1}) = \tan^{-1}\frac{-|\nabla_h b|^2}{f^2 N^2}, \tag{4.4}$$

and

$$\phi_{\mathrm{Ri_b}} < \phi_c = \tan^{-1}(-\zeta_g/f), \tag{4.5}$$

where $\zeta_g = f + \nabla \times \mathbf{u}_g$ and $\mathbf{u}_g$ is the geostrophic velocity. When $180^\circ < \phi_{\mathrm{Ri_b}} < -135^\circ$, the potential vorticity is negative due to unstable stratification and convective instability is expected to dominate. When $-135^\circ < \phi_{\mathrm{Ri_b}} < -90^\circ$, the potential vorticity is negative due to both unstable stratification and horizontal buoyancy gradients and so a hybrid convective/symmetric mode is predicted. For stable stratification and cyclonic vorticity $-90^\circ < \phi_{\mathrm{Ri_b}} < \phi_c$, with $\phi_c < -45^\circ$ implies that a symmetric instability should arise. For anti-cyclonic vorticity a symmetric mode is expected to dominate where $90^\circ < \phi_{\mathrm{Ri_b}} < -45^\circ$ and a hybrid symmetric-centrifugal instability is anticipated where $-45^\circ < \phi_{\mathrm{Ri_b}} < \phi_c$.

It is cautioned that this analysis does not take into account the vertical velocity shear that arises due to surface waves. Haney et al. (Subm. to JPO) show that wind and waves in the same direction leads to an increase in Ri_b. The balanced Richardson number here also assumes that there is no curvature to the flow.

Fig. 16 (upper panel) shows that up to 30% of the mixed layer volume is unstable to pure or hybrid symmetric instabilities in winter. The proportion of the mixed layer volume where such a condition holds grows somewhat as the resolution is made finer, though the values are comparable across all resolutions. In the shallow mixed layers early in the restratification period (April–August in Fig. 16, upper panel) very little negative potential vorticity is found at any resolution due to the stratifying effect of the surface heating. The proportion of the domain where negative potential vorticity is found then grows in late summer (September–October in Fig. 16, upper panel). It reaches its peak value quite early in the winter by November at all resolutions before gradually decreasing in late winter despite the continual cooling.

The vertical distribution of negative potential vorticity is shown in Fig. 16 (lower panels) and is similar at all resolutions. The lower panels shows that the occurrence of negative potential vorticity is essentially limited to the mean mixed layer. The distribution of negative potential vorticity is not concentrated in the Ekman layer reflecting the tendency for down-front winds to induce vertical mixing and so extract potential vorticity throughout the mixed layer (Thomas and Ferrari, 2008) when using *KPP*, though simulations with resolved boundary layer turbulence show that the extraction of potential vorticity may be concentrated in a shallower layer (Hamlington et al., 2014; Taylor and Ferrari, 2010). The peak proportion of the mixed layer volume that is most unstable to centrifugal instability grows from 1% of the mixed layer volume at the coarsest resolution to 4% at the finest resolution (not shown). In addition, the upper 10 m of the model domain develops a slight negative stratification in the cooling

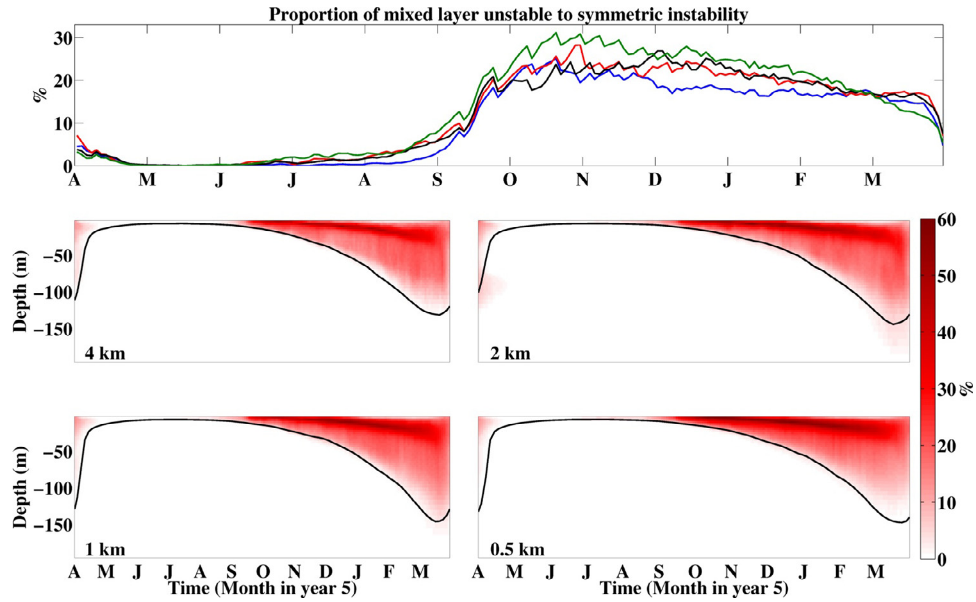

Fig. 16. The proportion of the domain with negative potential vorticity where a pure or hybrid symmetric mode is predicted. (Top panel) The mean proportion of the mixed layer volume where symmetric instability is predicted. (Lower panels) The proportion of the levels where symmetric instability is predicted. Calculated based on snapshot model outputs taken at 2-day intervals during the fifth year of the simulation. The black line in the lower panels is the mean mixed layer depth.

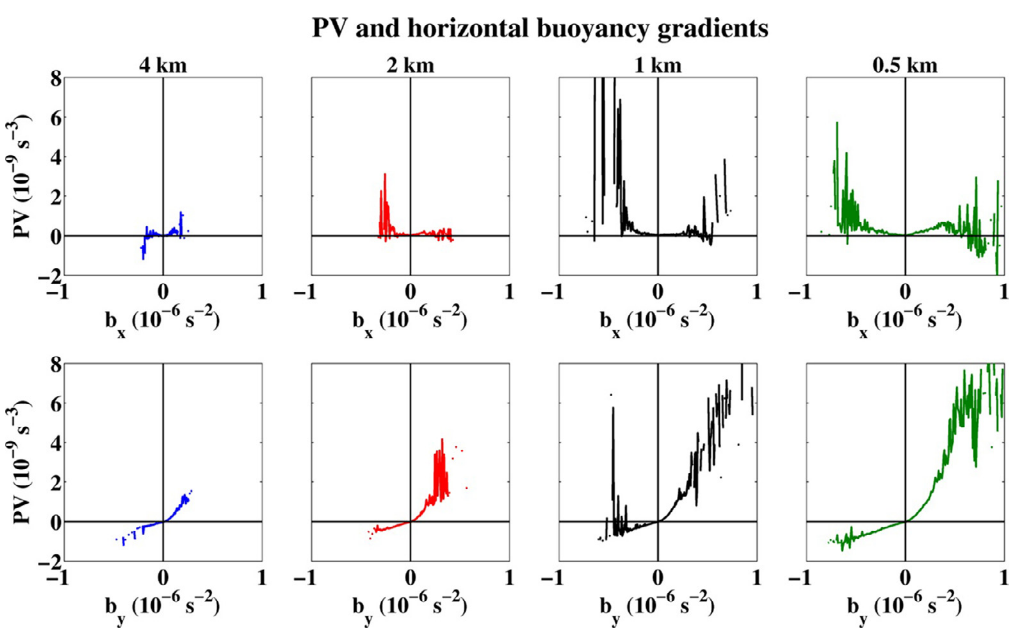

Fig. 17. The mean potential vorticity for a given horizontal buoyancy gradient at 9 m depth at in late December. (Top row) The mean potential vorticity for a given zonal buoyancy gradient. (Bottom row) The mean potential vorticity for a given meridional buoyancy gradient. These results are consistent with Fig. 11 of Capet et al. (2008b).

period at all resolutions. This negative stratification in the upper levels is a typical feature of numerical simulations.

As for Capet et al. (2008b), regions of negative potential vorticity are produced by the down-front wind mechanism driven by the zonal wind stress. Fig. 17 shows the mean potential vorticity for a given zonal or meridional buoyancy gradient based on a snapshot of model output at the end of December in year 5 at 9 m depth. The top row in Fig. 17 shows no systematic relationship between the zonal buoyancy gradient and potential vorticity. However, the bottom row shows that there is a near-linear relationship between the meridional buoyancy gradient and potential vorticity at all resolutions. When $b_y < 0$, colder water lies to the north of warmer water. Given the mean zonal wind, $b_y < 0$ corresponds to a down-front wind (Thomas, 2005) and mean potential vorticity is indeed negative in this case. On the other hand, where $b_y > 0$ the wind is up-front and mean potential vorticity is positive in this case. This effect becomes stronger as the resolution is made finer (Fig. 17, lower panels). The seasonal cycle in the proportion of the mixed layer unstable to symmetric instability (Fig. 16, upper panel) partly reflects the seasonal cycle in horizontal buoyancy gradients. When horizontal buoyancy gradients are stronger in the late summer and autumn (Fig. 6) the conditions for symmetric instability are most commonly found. As the horizontal buoyancy gradients weaken in late winter, less symmetric instability is expected.

A similar analysis can be carried out as in Fig. 17 where the potential vorticity is compared to the Okubo–Weiss parameter $S^2 - \zeta_z^2$, where $S^2 = (v_x + u_y)^2 + (u_x - v_y)^2$ is the strain. No systematic relationship between the Okubo–Weiss parameter and potential vorticity is found (not shown). This can be understood by considering the

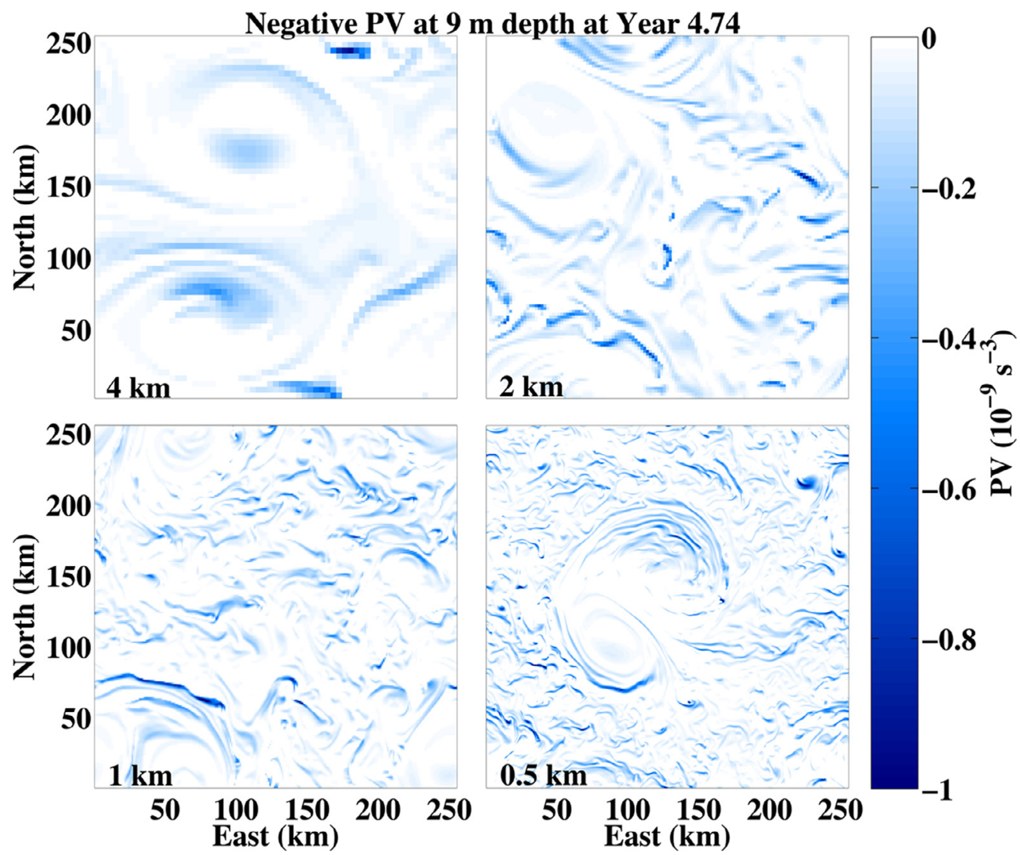

Fig. 18. Plan-view plots of negative potential vorticity at 9 m depth in late December at the indicated resolution. The colorscale saturates at $q = 0$ so regions of positive potential vorticity are shown in white.

horizontal distribution of negative potential vorticity at the end of December in Fig. 18. This figure illustrates that negative values of potential vorticity are found both inside as well as outside the vortices, for example at (100 km, 80 km) at 4 km resolution in the upper-left panel or at (110 km, 160 km) in the lower-right panel. Negative potential vorticity in the large vortices correspond to regions of negative meridional buoyancy gradients within the vortices. A forthcoming paper (Brannigan, in prep.) shows that the negative potential vorticity within the vortices leads to strong symmetric instabilities there.

4.4. Vertical advective fluxes

The magnitude of the vertical buoyancy fluxes is $\overline{w'b'}$, where w is the vertical velocity, b is the buoyancy and primes indicate a departure from the level mean. The second panel in Fig. 19 shows that vertical buoyancy fluxes averaged over the mixed layer become stronger as the resolution becomes finer and has its peak in December and January. As such the seasonal cycle in vertical advective fluxes differs from the diagnosed seasonal cycle in frontogenesis and Ekman buoyancy fluxes. The lower panels in Fig. 19 show the vertical profiles of $\overline{w'b'}$ and show that the most intense vertical fluxes occur in December, when the mean mixed layer is just 55 m deep. This is the same time period that the slope of the surface velocity power spectral density arrives at its winter value close to -2 (Fig. 8). There are negative vertical buoyancy fluxes below the mean mixed layer throughout the year. An initial hypothesis is that the negative vertical buoyancy fluxes arise due to the spatial structure of the wind forcing employed. However, the negative vertical buoyancy fluxes are present if the model is forced only with the uniform zonal wind after it has been spun up and so the spatial structure of the wind forcing can be ruled out as the cause of the negative buoyancy fluxes. These negative buoyancy fluxes appear to be associated with regions of negative potential vorticity and are investigated further in a forthcoming paper.

The analysis in Section 4.3 shows that up to 30% of the mixed layer experiences negative potential vorticity during the winter. Thus the majority of the mixed layer has positive potential vorticity and so mixed layer baroclinic instabilities are expected to be the dominant component of the vertical advective fluxes (Bachman and Fox-Kemper, 2013; Boccaletti et al., 2007; Brüggemann and Eden, 2014; Fox-Kemper et al., 2008; Molemaker et al., 2005; Skyllingstad and Samelson, 2012; Stone, 1966). The importance of these instabilities can be estimated through the seasonal cycle by scaling the potential energy available for release. We employ the central concept of the Fox-Kemper et al. (2008) parameterisation by estimating the magnitude of the available potential energy

$$\mathrm{APE} = H^2|\nabla_h b|, \tag{4.6}$$

where H is the mixed layer depth. This is shown in Fig. 19 (top panel) where the seasonal cycle in APE is somewhat different than that of the vertical buoyancy fluxes, as the vertical buoyancy fluxes peak earlier in winter than the APE. The peak in vertical buoyancy fluxes before the peak in APE could reflect other factors such as the effect of strain on the growth of baroclinic instability (Bishop, 1993; McWilliams and Molemaker, 2011; Spall, 1997), as some of the highest APE is found in the confluence region between mesoscale eddies where the fronts do not have meanders indicative of baroclinic waves. An example of this is the straight front that runs along $y = 75$ km in the lower-left panel of Fig. 5. Flow curvature could also affect the growth of baroclinic eddies, as the APE metric is high in and around cyclonic eddies, where again there is limited evidence that baroclinic instability occurring, for example around the cyclonic eddy centred at (250 km, 40 km) in the lower-right panel of Fig. 5.

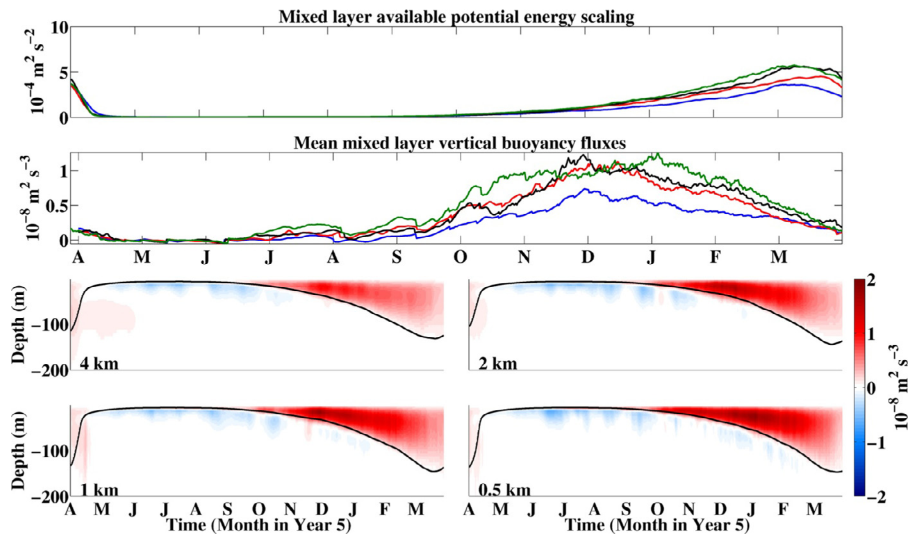

Fig. 19. The available potential energy and the mean vertical advective buoyancy flux $\overline{w'b'}$ over the fifth year of the simulations. (Upper panel) The mean available potential energy in the mixed layer $\overline{APE} = \overline{H^2|\nabla_h b|}$ at 12 h intervals, where H is the mixed layer depth. (Second panel) The flux integrated over the mean mixed layer with a colour scheme as for Fig. 4. (Lower panels) The vertical profile of the mean vertical advective fluxes at the resolution indicated. The vertical flux is averaged by model level and in six-hour intervals online. The black line in the lower panels shows the mean mixed layer depth at that time.

5. Discussion

The results of a series of multi-year simulations in a domain analogous to the mid-latitude open ocean show a significant seasonal cycle in submesoscale flows and this seasonal cycle becomes more pronounced as the resolution is made finer. The slopes of horizontal spectra of SST and surface velocity are steep in summer when the mixed layer is less than 20 m deep and then rapidly become shallower as the mixed layer deepens. The shallowing of the velocity spectra stops when the mixed layer is just 40 m deep, suggesting that the dynamical regime reflected by this shallower slope does not require particularly deep mixed layers.

The simulations also vary across the range of resolutions. As the resolution is increased, sharper fronts emerge and the residual momentum balance of the flow includes a larger contribution from advective and rapidly-developing motions. Processes at ocean fronts including frontogenesis and Ekman buoyancy fluxes are found to strengthen as the resolution is made finer. The prevalence of negative potential vorticity does not increase monotonically with resolution, but instead depends on the flow configuration at a given time. The stronger frontogenetical processes lead to more available potential energy as the resolution is made finer and stronger advective vertical buoyancy fluxes in winter.

Both available potential energy and vertical buoyancy fluxes in the mixed layer are stronger in winter and so we conclude that overturning instabilities such as baroclinic instability or symmetric instability are the primary driver of these vertical buoyancy fluxes, rather than the fluxes associated with frontogenesis or Ekman pumping. Mixed layer vertical buoyancy fluxes peak in mid-winter, while the available potential energy peaks in late winter. This may reflect other factors such as strain, vorticity or curvature (Bishop, 1993; McWilliams and Molemaker, 2011; Spall, 1997; Thomas, 2012) that affect stability in addition to horizontal buoyancy gradients. The different seasonal cycles between the vertical buoyancy fluxes and frontogenesis suggests that the balance between frontogenesis and mixed layer baroclinic instabilities (e.g. McWilliams and Molemaker, 2011) may be quite sensitive to the vertical scale height with frontogenesis stronger when the mixed layer is shallow and baroclinic instabilities stronger as the mixed layer deepens for a given horizontal buoyancy gradient and strain.

Recent numerical and observational studies also find that the spectral slope of velocity in the mixed layer shallows in winter (Callies et al., 2015; Mensa et al., 2013; Sasaki et al., 2014). These studies interpret this result as the consequence of frontogenesis and mixed layer baroclinic instabilities considered by Boccaletti et al. (2007). However, the results in Section 4.3 show that 30% of the mixed layer volume has negative potential vorticity and is therefore most unstable to symmetric instability. As such, it is possible that the submesoscale length range is energised by symmetric instability in addition to baroclinic instability and frontogenesis. Extensive symmetric instability could have implications for describing mixed layer flows in terms of quasi-geostrophic or surface quasi-geostrophic models, as the flow associated with symmetric instability is unbalanced (Stone, 1966) and so cannot be captured by theories based on balanced dynamics in their standard forms.

The question of convergence of the simulations over this range of resolutions remains open. The similar seasonal cycle in spectral slopes in the three finer resolution cases can be used to argue for convergence, as per Capet et al. (2008a). However, the diagnosed submesoscale processes continue to become stronger as the resolution is made finer and the mean stratification profile varies throughout the range of resolutions employed in Fig. 4. Furthermore, Bachman and Taylor (2014) show that the degree to which symmetric instability is resolved changes markedly over this range of resolutions and so this also affects the subsequent development of stratification as the resolution is refined. The inclusion of surface waves and Langmuir turbulence also significantly affects the vertical fluxes and stratification (Hamlington et al., 2014; Haney et al., Subm. to JPO).

The results show that some departures from geostrophic balance are found in the domain. In particular, there is a departure from geostrophy in the mixed layer of the large vortices where non-linear effects due to the centripetal acceleration should also be taken into account, in agreement with the results of Douglass and Richman (2015). The model solutions also show that the momentum balance in the mixed layer includes a component due to the vertical diffusion of momentum, though a more accurate description requires taking into account the physics of the unresolved processes (Hamlington et al., 2014; McWilliams and Fox-Kemper, 2013; Taylor and Ferrari, 2010).

There are of course a number of limitations to this study in addition to those discussed above such as the artificial structure of the wind forcing. The grid resolutions employed require the use of a vertical mixed layer parameterisation and so important effects like the convective layer depth (Taylor and Ferrari, 2010; Thomas et al., 2013), interaction with small-scale turbulence (Skyllingstad and Samelson, 2012), or surface wave effects (Hamlington et al., 2014; Haney et al., Subm. to JPO; McWilliams and Fox-Kemper, 2013) could not be explored. The surface boundary conditions are imposed and so do not allow SST anomalies to generate differential air-sea fluxes. In addition, it is often the case that the the internal wave field in such model studies is less energetic than in the real ocean (Shcherbina et al., 2013), due to the wind forcing being sub-inertial and the lack of tides and topography (Callies and Ferrari, 2013). The contribution of the time derivative terms to the residual balance shows, however, that internal waves are generated due to unbalanced motions (Shakespeare and Taylor, 2013).

To follow on from this work, the presence of submesoscale filaments inside mesoscale vortices will be examined in more detail (Brannigan, in prep.). The development of stratification in the model as the resolution varies will also be investigated to illustrate why a deeper mixed layer develops at finer resolution. These predictions will also be tested with the OSMOSIS mooring array from the North Atlantic.

Acknowledgements

This work forms part of the OSMOSIS project funded by the Natural Environment Research Council (grant no. NE/I019921/1). We thank David Munday for assistance with running the experiment. The responses of Baylor Fox-Kemper and two anonymous reviewers have greatly improved the manuscript along with helpful comments from Andy Thompson, Ayah Lazar, Andy Hogg, Joern Callies and our colleagues in the OSMOSIS consortium. This work used the ARCHER UK National Supercomputing Service.

Supplementary material

Supplementary material associated with this article can be found, in the online version, at 10.1016/j.ocemod.2015.05.002

References

Arbic, B.K., Scott, R.B., 2008. On quadratic bottom drag, geostrophic turbulence, and oceanic mesoscale eddies. J. Phys. Oceanogr. 38 (1), 84–103.
Bachman, S., Fox-Kemper, B., 2013. Eddy parameterization challenge suite I: eady spindown. Ocean Modell. 64, 12–28. doi:10.1016/j.ocemod.2012.12.003. http://linkinghub.elsevier.com/retrieve/pii/S1463500312001801
Bachman, S., Taylor, J., 2014. Modelling of partially-resolved oceanic symmetric instability. Ocean Modell. 82, 15–27. doi:10.1016/j.ocemod.2014.07.006. http://linkinghub.elsevier.com/retrieve/pii/S1463500314000961
Belcher, S.E., Grant, A.L., Hanley, K.E., Fox-Kemper, B., Van Roekel, L., Sullivan, P.P., Large, W.G., Brown, A., Hines, A., Calvert, D., 2012. A global perspective on langmuir turbulence in the ocean surface boundary layer. Geophys. Res. Lett. 39 (18).
Berry, D.I., Kent, E.C., 2009. A new air-sea interaction gridded dataset from icoads with uncertainty estimates. Bull. Am. Meteorol. Soc. 90 (5), 645–656.
Bishop, C.H., 1993. On the behaviour of baroclinic waves undergoing horizontal deformation. II: error [U+2010] blind amplification and Rossy wave diagnostics. Q.J.R. Meteorol. Soc. 119 (510), 241–267.
Boccaletti, G., Ferrari, R., Fox-Kemper, B., 2007. Mixed layer instabilities and restratification. J. Phys. Oceanogr. 37 (9), 2228–2250. doi:10.1175/JPO3101.1. http://journals.ametsoc.org/doi/abs/10.1175/JPO3101.1
Brannigan, L., Intense upwelling in mesoscale eddies. in prep.
Brüggemann, N., Eden, C., 2014. Evaluating different parameterizations for mixed layer eddy fluxes induced by baroclinic instability. J. Phys. Oceanogr. 44 (9), 2524–2546.
Callies, J., Ferrari, R., 2013. Interpreting energy and tracer spectra of upper-ocean turbulence in the submesoscale range (1200 km). J. Phys. Oceanogr. 43 (11), 2456–2474.
Callies, J., Ferrari, R., Klymak, J.M., Mol, 2015. Seasonality in submesoscale turbulence. Nat. Commun. In press.
Capet, X., McWilliams, J., Molemaker, M., Shchepetkin, A., 2008a. Mesoscale to submesoscale transition in the California current system. Part I: flow structure, eddy flux, and observational tests. J. Phys. Oceanogr. 38 (1), 29–43.
Capet, X., McWilliams, J., Molemaker, M., Shchepetkin, A., 2008b. Mesoscale to submesoscale transition in the California current system. Part II: frontal processes. J. Phys. Oceanogr. 38 (1), 44–64.
Capet, X., McWilliams, J., Molemaker, M., Shchepetkin, A., 2008c. Mesoscale to submesoscale transition in the California current system. Part III: energy balance and flux. J. Phys. Oceanogr. 38 (10), 2256–2269.
Dale, A.C., Barth, J.A., Levine, M.D., Austin, J.A., 2008. Observations of mixed layer restratification by onshore surface transport following wind reversal in a coastal upwelling region. J. Geophys. Res. 113 (C1), C01010. doi:10.1029/2007JC004128. http://doi.wiley.com/10.1029/2007JC004128
Damerell, G.M., Heywood, K.J., Binetti, U., Kaiser, J., Thompson, A.F., in prep. for Geophys.Res.Lett.Upper ocean variability at the Porcupine Abyssal Plain time series site during 2012–2013.
D'Asaro, E., Lee, C., Rainville, L., Harcourt, R., Thomas, L., 2011. Enhanced turbulence and energy dissipation at ocean fronts. Science 332 (6027), 318–322.
Douglass, E.M., Richman, J.G., 2015. Analysis of ageostrophy in strong surface eddies in the atlantic ocean. J. Geophys. Res. Oceans 120 (3), 1490–1507. http://dx.doi.org/10.1002/2014JC010350
Fox-Kemper, B., Ferrari, R., Hallberg, R., 2008. Parameterization of mixed layer Eddies. Part I: theory and diagnosis. J. Phys. Oceanogr. 38 (6), 1145–1165. doi:10.1175/2007JPO3792.1. http://journals.ametsoc.org/doi/abs/10.1175/2007JPO3792.1
Fox-Kemper, B., Menemenlis, D., 2013. Can large eddy simulation techniques improve mesoscale rich ocean models? In: Ocean Modeling in an Eddying Regime. American Geophysical Union, pp. 319–337. http://dx.doi.org/10.1029/177GM19.
Graham, J.P., Ringler, T., 2013. A framework for the evaluation of turbulence closures used in mesoscale ocean large-eddy simulations. Ocean Modell 65, 25–39.
Grant, A.L.M., Belcher, S.E., 2009. Characteristics of Langmuir turbulence in the ocean mixed layer. J. Phys. Oceanogr. 39 (8), 1871–1887. doi:10.1175/2009JPO4119.1. http://journals.ametsoc.org/doi/abs/10.1175/2009JPO4119.1
Griffies, S.M., Hallberg, R.W., 2000. Biharmonic friction with a Smagorinsky-like viscosity for use in large-scale eddy-permitting ocean models. Mon. Weather Rev. 128 (8), 2935–2946.
Gula, J., Molemaker, M.J., McWilliams, J.C., 2014. Submesoscale cold filaments in the gulf stream. J. Phys. Oceanogr. 44 (10), 2617–2643. doi:10.1175/JPO-D-14-0029.1. http://journals.ametsoc.org/doi/abs/10.1175/JPO-D-14-0029.1
Haine, T.W.N., Marshall, J., 1998. Gravitational, symmetric, and baroclinic instability of the ocean mixed layer. J. Phys. Oceanogr. 28 (4), 634–658.
Hamlington, P.E., Van Roekel, L.P., Fox-Kemper, B., Julien, K., Chini, G.P., 2014. Langmuir-submesoscale interactions: descriptive analysis of multiscale frontal spindown simulations. J. Phys. Oceanogr. 44 (9), 2249–2272. doi:10.1175/JPO-D-13-0139.1. http://journals.ametsoc.org/doi/abs/10.1175/JPO-D-13-0139.1
Haney, S., Bachman, S., Cooper, B., Kupper, S., McCaffrey, K., Van Roekel, L., Stevenson, S., Fox-Kemper, B., Ferrari, R., 2012. Hurricane wake restratification rates of one-, two- and three-dimensional processes. J. Mar. Res. 70 (6), 824–850.
Haney, S., Fox-Kemper, B., Julien, K., Webb, A., Subm. to JPO. Symmetric and Geostrophic Instabilities in the Wave-Forced Ocean Mixed Layer.
Hill, C., Ferreira, D., Campin, J.-M., Marshall, J., Abernathey, R., Barrier, N., 2012. Controlling spurious diapycnal mixing in eddy-resolving height-coordinate ocean models - Insights from virtual deliberate tracer release experiments. Ocean Modell. 45-46, 14–26.
Hosegood, P., Gregg, M.C., Alford, M.H., 2006. Sub-mesoscale lateral density structure in the oceanic surface mixed layer. Geophys. Res. Lett. 33 (22), L22604. doi:10.1029/2006GL026797. http://doi.wiley.com/10.1029/2006GL026797
Hoskins, B.J., Bretherton, 1972. Atmospheric frontogenesis models - Mathematical formulation and solution. J. Atmos. Sci. 29 (1), 11–37.
Ilicak, M., Adcroft, A.J., Griffies, S.M., Hallberg, R.W., 2012. Spurious dianeutral mixing and the role of momentum closure. Ocean Modell. 45-46, 37–58.
Koszalka, I., Bracco, A., McWilliams, J.C., Provenzale, A., 2009. Dynamics of wind-forced coherent anticyclones in the open ocean. J. Geophys. Res. 114 (C8), C08011. doi:10.1029/2009JC005388. http://doi.wiley.com/10.1029/2009JC005388
Lapeyre, G., Klein, P., Hua, B.L., 2006. Oceanic restratification forced by surface frontogenesis. J. Phys. Oceanogr. 36 (8), 1577–1590.
Large, W.G., McWilliams, J.C., Doney, S.C., 1994. Oceanic vertical mixing - a review and a model with a nonlocal boundary-layer parameterization. Rev. Geophys. 32 (4), 363–403.
Leith, C.E., 1996. Stochastic models of chaotic systems. Physica D 98 (2-4), 481–491.
Lévy, M., Klein, P., Tréguier, a.-M., Iovino, D., Madec, G., Masson, S., Takahashi, K., 2010. Modifications of gyre circulation by sub-mesoscale physics. Ocean Modell. 34 (1-2), 1–15. doi:10.1016/j.ocemod.2010.04.001. http://linkinghub.elsevier.com/retrieve/pii/S1463500310000582
Mahadevan, A., 2006. Modeling vertical motion at ocean fronts: are nonhydrostatic effects relevant at submesoscales? Ocean Modell. 14 (3-4), 222–240.
Mahadevan, A., Tandon, A., Ferrari, R., 2010. Rapid changes in mixed layer stratification driven by submesoscale instabilities and winds. J. Geophys. Res. Oceans 115, C03017.
Marshall, J., Adcroft, A., Hill, C., Perelman, L., Heisey, C., 1997. A finite-volume, incompressible Navier stokes model for studies of the ocean on parallel computers. J. Geophys. Res. Oceans 102 (C3), 5753–5766.
Marshall, J., Schott, F., 1999. Open ocean convection: observations, theory, and models. Rev. Geophys. 37 (1), 1–64.
McWilliams, J.C., Fox-Kemper, B., 2013. Oceanic wave-balanced surface fronts and filaments. J. Fluid Mech. 730, 464–490.
McWilliams, J.C., Molemaker, M.J., 2011. Baroclinic frontal arrest: a sequel to unstable frontogenesis. J. Phys. Oceanogr. 41 (3), 601–619. doi:10.1175/2010JPO4493.1. http://journals.ametsoc.org/doi/abs/10.1175/2010JPO4493.1
Mensa, J.A., Garraffo, Z., Griffa, A., Özgökmen, T.M., Haza, A., Veneziani, M., 2013. Seasonality of the submesoscale dynamics in the Gulf stream region. Ocean Dyn. 63 (8), 923–941. doi:10.1007/s10236-013-0633-1. http://link.springer.com/10.1007/s10236-013-0633-1

Molemaker, M.J., McWilliams, J.C., Yavneh, I., 2005. Baroclinic instability and loss of balance. J. Phys. Oceanogr. 35 (9), 1505–1517.
Nastrom, G., Gage, K.S., 1985. A climatology of atmospheric wavenumber spectra of wind and temperature observed by commercial aircraft. J. Atmos. Sci. 42 (9), 950–960.
Nurser, A.J.G., Zhang, J.W., 2000. Eddy-induced mixed layer shallowing and mixed layer/thermocline exchange. J. Geophys. Res. 105 (C9), 21851–21868. http://dx.doi.org/10.1029/2000JC900018
Painter, S.C., Pidcock, R.E., Allen, J.T., 2010. A mesoscale eddy driving spatial and temporal heterogeneity in the productivity of the euphotic zone of the northeast Atlantic. Deep Sea Res. Part II: Top. Stud. Oceanogr. 57 (15), 1281–1292.
Prather, M.J., 1986. Numerical advection by conservation of second order moments. J. Geophys. Res.: Atmos. (1984–2012) 91 (D6), 6671–6681.
Price, J.F., Weller, R.A., Pinkel, R., 1986. Diurnal cycling - observations and models of the upper ocean response to Diurnal heating, cooling, and wind mixing. J. Geophys. Res. Oceans 91 (C7), 8411–8427.
Ramachandran, S., Tandon, A., Mahadevan, A., 2013. Effect of subgrid-scale mixing on the evolution of forced submesoscale instabilities. Ocean Modell. 66, 45–63.
Samelson, R.M., 1993. Linear instability of a mixed-layer front. J. Geophys. Res. 98 (C6), 10195–10204. http://dx.doi.org/10.1029/93JC00457
Sasaki, H., Klein, P., Qiu, B., Sasai, Y., 2014. Impact of oceanic-scale interactions on the seasonal modulation of ocean dynamics by the atmosphere. Nat. Commun. 5. http://dx.doi.org/10.1038/ncomms6636
Shakespeare, C.J., Taylor, J.R., 2013. A generalised mathematical model of geostrophic adjustment and frontogenesis: uniform potential vorticity. J. Fluid Mech. 736, 366–413.
Shcherbina, A.Y., D'Asaro, E.A., Lee, C.M., Klymak, J.M., Molemaker, M.J., McWilliams, J.C., 2013. Statistics of vertical vorticity, divergence, and strain in a developed submesoscale turbulence field. Geophys. Res. Lett. 40 (17), 4706–4711.
Skyllingstad, E.D., Samelson, R., 2012. Baroclinic frontal instabilities and turbulent mixing in the surface boundary layer. Part I: unforced simulations. J. Phys. Oceanogr. 42 (10), 1701–1716.
Smagorinsky, J., 1963. General circulation experiments with the primitive equations: I. The basic experiment. Mon.Weather Rev. 91 (3), 99–164.
Spall, M.A., 1997. Baroclinic jets in confluent flow. J. Phys. Oceanogr. 27 (6), 1054–1071.
Stone, P.H., 1966. On non-geostrophic baroclinic stability. J. Atmos. Sci. 23 (4), 390–400.
Sutherland, G., Christensen, K.H., Ward, B., 2014. Evaluating Langmuir turbulence parameterizations in the ocean surface boundary layer. J. Geophys. Res. Oceans 119 (3), 1899–1910.
Tandon, A., Garrett, C., 1994. Mixed-layer restratification due to a horizontal density gradient. J. Phys. Oceanogr. 24 (6), 1419–1424.
Taylor, J.R., Ferrari, R., 2010. Buoyancy and wind-driven convection at mixed layer density fronts. J. Phys. Oceanogr. 40 (6), 1222–1242. doi:10.1175/2010JPO4365.1. http://journals.ametsoc.org/doi/abs/10.1175/2010JPO4365.1
Thomas, L., Ferrari, R., 2008. Friction, frontogenesis, and the stratification of the surface mixed layer. J. Phys. Oceanogr. 38 (11), 2501–2518. doi:10.1175/2008JPO3797.1. http://journals.ametsoc.org/doi/abs/10.1175/2008JPO3797.1
Thomas, L.N., 2005. Destruction of potential vorticity by winds. J. Phys. Oceanogr. 35 (12), 2457–2466.
Thomas, L.N., 2012. On the effects of frontogenetic strain on symmetric instability and inertia–gravity waves. J. Fluid Mech. 711, 620–640. doi:10.1017/jfm.2012.416. http://www.journals.cambridge.org/abstract_S0022112012004168
Thomas, L.N., Taylor, J.R., 2010. Reduction of the usable wind-work on the general circulation by forced symmetric instability. Geophys. Res. Lett. 37 (18). doi:10.1029/2010GL044680. http://doi.wiley.com/10.1029/2010GL044680
Thomas, L.N., Taylor, J.R., Ferrari, R., Joyce, T.M., 2013. Symmetric instability in the gulf stream. Deep Sea Res. Part II: Top. Stud. Oceanogr. 91, 96–110. doi:10.1016/j.dsr2.2013.02.025. http://linkinghub.elsevier.com/retrieve/pii/S0967064513000829
Thomsen, S., Eden, C., Czeschel, L., 2013. Stability analysis of the labrador current. J. Phys. Oceanogr. 44 (2), 445–463. doi:10.1175/JPO-D-13-0121.1.